ISSN 1063-7745, Crystallography Reports, 2024, Vol. 69, No. 1, pp. 65–72. © Pleiades Publishing, Inc., 2024.

SURFACE AND THIN FILMS

Dedicated to the 300th anniversary of St. Petersburg State University

Structure and Electrical Conductivity of Thin AlN Films on Si

N. V. Bazlov[a,b,*], O. F. Vyvenko[a], N. V. Niyazova[b], I. M. Kotina[b], M. V. Trushin[b], and A. S. Bondarenko[a]

[a] *Physics Department, St. Petersburg State University, St. Petersburg, Petrodvorets, 198504 Russia*

[b] *St. Petersburg Nuclear Physics Institute, National Research Centre "Kurchatov Institute," Gatchina, Leningrad oblast, 188300 Russia*

**e-mail: nikolay.bazlov@gmail.com*

Received June 8, 2023; revised June 8, 2023; accepted June 27, 2023

Abstract—Aluminum nitride films have been synthesized by reactive magnetron sputtering on *n*-Si(100) substrates. AlN layers with thicknesses from 2 to 150 nm were obtained to establish a correlation between the structure of the films and their electrical conductivity. Electron microscopy revealed that the amorphous structure of the films passes to nanocrystalline one while moving away from the substrate surface. Films with thicknesses below 20 nm had a high conductivity: up to 10 $(\Omega\ \text{cm})^{-1}$; with an increase in thickness the conductivity dropped to 10^{-7} $(\Omega\ \text{cm})^{-1}$. The high conductivity of thin AlN layers is believed to be due to the high density of the boundaries of grains built-in into amorphous matrix.

DOI: 10.1134/S1063774523601260

INTRODUCTION

Silicon surface-barrier detectors of nuclear radiation based on Schottky barriers Al–(*p*-Si) exhibit variability of working parameters during their operation. One of possible solutions to this problem implies introduction of a tunnel-transparent aluminum nitride (AlN) layer between the metal contact and semiconductor [1, 2]. It was shown in [1] that metal–AlN–(*p*-Si) structures are characterized by higher temporal stability and lower leakage currents in comparison with Schottky barriers. At the same time, the nature of the states at the AlN–(*p*-Si) interface and the mechanisms of current transport in an AlN film, which are responsible for charge losses and level of low-frequency noise in the detector, have been studied insufficiently well to formulate recommendations for optimizing the manufacturing technologies of the aforementioned structures.

An important condition for the manufacturing technology of such structures is sufficiently low substrate temperature, at which thermal defects are not generated in it, and diffusion of impurity atoms through interfaces is absent. This condition can be fulfilled using reactive magnetron sputtering (RMS). A number of works have been devoted to the analysis of growth conditions for AlN films formed by RMS on the surface of silicon substrates. Generally, these films are nanocrystalline ones; they have a wurtzite structure, high density, and a well-developed columnar structure with grains from several nanometers to several tens of nanometers in diameter. In correspondence with the generally accepted point of view, a necessary condition for growing an oriented film is the high mobility of adatoms: having a sufficient kinetic energy, these atoms can occupy thermodynamically equilibrium sites [3–7]. The mobility of adatoms is provided by high substrate temperature and energy transfer from the atoms and ions adsorbed on the surface. At a low substrate temperature and relatively low preliminary vacuum in the chamber, which are often caused by technological features, the quality of grown AlN films is deteriorated. This deterioration manifests itself in the reduction of the orientational order of grains and formation of an amorphous layer between the substrate and film bulk [8–11]. As was established in [12], an amorphous aluminum nitride layer several nanometers thick may arise at low substrate temperatures even when the growth chamber is preliminarily pumped to ultrahigh vacuum. At low adatom energies the formation of an amorphous layer facilitates lattice matching between the substrate and nanocrystalline film. A correct choice of the working pressure in the chamber, gas mixture composition, magnetron–substrate distance, and magnetron power may compensate for the effect of low substrate temperature and provide formation of high-quality nanocrystalline AlN films [7]. As follows from the results of [4–6, 9, 11, 13–17], there is a wide range of parameters for

standard RMS systems, in which growth occurs under conditions close to thermodynamical equilibrium, and the *c* axis of deposited AlN films is oriented perpendicular to the substrate surface, independent of the substrate type. The optimal values of the aforementioned parameters were estimated in [3–6, 10, 13–16, 18, 19].

However, the main reason for the occurrence of an amorphous layer during growth of AlN films in vacuum chambers of standard RMS systems is the presence of residual oxygen [9, 16]. As compared with nitrogen, oxygen has a much higher chemical activity in compounds with aluminum. The changes in the Gibbs free energies for the reactions of formation of AlN and Al_2O_3 are, respectively, −253 and −1480 kJ/mol [9], which makes oxidation much more preferred than nitride formation. The changes in the chemical composition and texture of AlN films with an increase in the distance from the substrate surface were investigated in [9, 20], where these changes were found to be due to the decrease in the substrate influence and reduction of the residual oxygen pressure during film growth. As was noted in [21], a change in the oxygen content in an AlN film may affect significantly its electrical properties, in particular, electrical conductivity.

There are only few works [21–24] where the electrical conductivity of AlN films deposited on silicon substrates was estimated. These estimates show that the RMS-produced AlN films with thicknesses exceeding several hundreds of nanometers are insulating and can be used as a gate insulator material with a high permittivity. Currently, there are no data in the literature on the conductivity of thinner AlN layers formed on silicon, whose texture and chemical composition are most strongly affected by residual oxygen.

In this study aluminum nitride films were synthesized by RMS on silicon substrates under the conditions close to optimal [4–6, 15, 16]. AlN layers with thicknesses from 2 to 150 nm were grown to establish a correlation between the structure and electrical conductivity of the films. The film morphology and structure were analyzed using a scanning electron microscope (SEM) and a transmission electron microscope (TEM). To minimize the bulk resistance of the formed structures and remove the surface compensated layer formed in *p*-Si as a result of acid etching (these factors impede electrical conductivity measurements), substrates were cut from low-resistivity *n*-Si wafers. The electrical conductivity of the films was estimated from the current–voltage (*I–U*) characteristics of metal–insulator–semiconductor (MIS) structures Au–AlN–(*n*-Si).

PREPARATION OF SAMPLES AND EXPERIMENTAL EQUIPMENT

AlN films were synthesized by means of a TORR vacuum system (TORR International, INC) with a magnetron operating in the ac current mode with a frequency of 13.56 MHz and specified power of 150 W. A gas mixture of nitrogen and argon with purities of 99.9999 and 99.998%, respectively, was used. The partial gas pressures were 2.5×10^{-3} Torr for nitrogen and 3.0×10^{-3} Torr for argon; they were maintained automatically using leak valves. The aluminum (purity of 99.9999%) target was 50.8 mm in diameter. The distance between the target and substrate during deposition was 50 mm. Silicon substrates were located on a holder and oriented normally to the plasma flow. During deposition the holder temperature was maintained equal to 250°C. The film thickness was measured using a calibrated piezoelectric sensor and then monitored with the aid of an electron microscope.

Substrates for film deposition were cut from wafers of degenerate *n*-Si with an upper moderately doped epitaxial layer. The thicknesses of the wafer and epitaxial *n*-Si(100) layer were, respectively, 650 and 5 μm; their resistivities were 0.025 and 5 Ω cm, respectively. Before deposition the substrates were etched in an aqueous solution of hydrofluoric acid ($HF : H_2O = 1 : 10$) for 1 min at room temperature to remove native oxide. After etching a substrate was placed on a mobile holder in the vacuum chamber; the holder was spaced from the magnetron and closed with a shutter. To remove molecules of adsorbed gases and water from the surface of substrates, the latter were kept in vacuum (1×10^{-5} Torr) at a temperature of 500°C for 30 min, after which the holder temperature was lowered to 250°C. The aluminum target surface was cleaned by supplying an argon flow corresponding to a pressure of 1.2×10^{-2} Torr, and the magnetron was switched on at power of 150 W. After the 5-min target cleaning, a nitrogen flow corresponding to a pressure of 2.5×10^{-3} Torr was supplied, and the partial argon pressure was reduced to 3×10^{-3} Torr. After the time necessary for establishing a stationary deposition rate at a level of 0.4 Å/s, the holder with a substrate was moved towards the magnetron, and the shutter was opened. When the film thickness reached the specified value, the magnetron was switched off, the gas supply was stopped, and the prepared sample was kept in vacuum for 15 min at a temperature of 250°C.

To form MIS structures, gold contacts 1.5 mm in diameter and 50 nm thick were deposited on the surface of prepared AlN films. Ohmic contacts were deposited on the rear side of the substrates using gallium–aluminum eutectics. Series of Au–AlN–(*n*-Si) structures with different film thicknesses (from 2 to 150 nm) were prepared in the same way. In addition, an initial Au–(*n*-Si) diode was fabricated from the same silicon wafer to measure the base resistance.

A lamella $500 \times 500 \times 50$ nm^3 in size was additionally cut from a sample with a 120-nm AlN film to perform a TEM study of the microstructure.

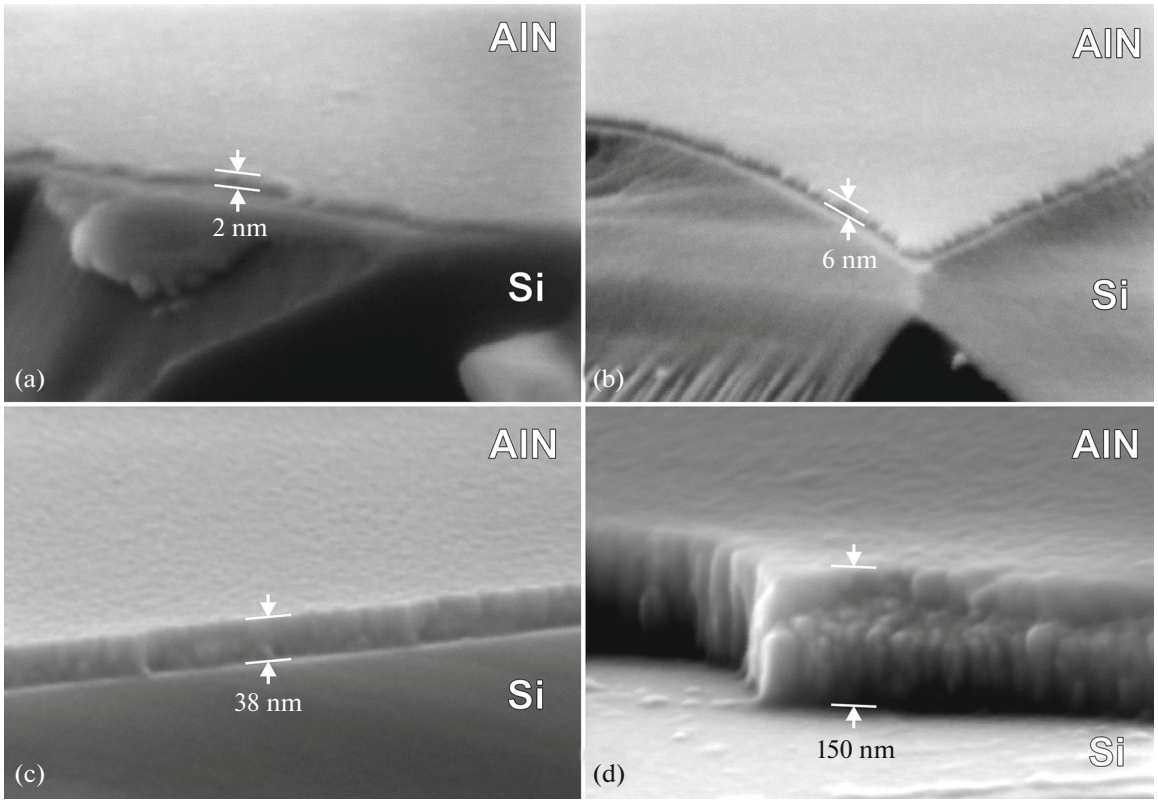

Fig. 1. SEM images of AlN films grown by RMS on *n*-Si(001) substrates. The films with thicknesses of (a) 2 and (b) 6 nm are continuous and amorphous, with nanocrystalline inclusions. The films with thicknesses of (c) 38 and (d) 150 nm are nanocrystalline, with a columnar texture.

The morphology and microstructure of deposited films were analyzed using a SEM Merlin (Carl Zeiss) and a TEM Libra 200 (Carl Zeiss). The *I*–*U* characteristics of fabricated MIS structures were measured using a Keithley 6517B electrometer.

MEASUREMENT RESULTS

Morphology and Microstructure Films

Figure 1 shows typical surface SEM images of samples with AlN film thicknesses equal to 2, 6, 38, and 150 nm. All deposited films, up to 2 nm thick, were continuous. As can be seen in the images, the morphology and texture of the films changed with a change in their thickness. Most of the volume of the thinnest films was occupied by amorphous phase (Figs. 1a, 1b). Nanocrystalline grains distributed over it had a size approximately equal to the film thickness. With an increase in the film thickness, the size of grains increased, the volume of the amorphous material between grains decreased, and the film acquired a columnar texture (Figs. 1c, 1d). As can be seen in Fig. 1d, the transverse grain size in thicker films increased from several nanometers to several tens of nanometers with an increase in the distance from the substrate surface.

Changes in the film structure with a change in the distance from the silicon substrate can be observed in the TEM image of the sample cross section obtained on a lamella (Fig. 2a). Near the silicon surface one can select amorphous layer I with a thickness ~10 nm, containing rare nanocrystalline grains ~5 nm in size. With an increase in the distance from the substrate, the grain density increases. In layer II amorphous and crystalline phases have comparable volumes; the grain size increases to 10 nm. In layer III, at distances from the substrate surface exceeding 30 nm, the nanocrystalline phase occupies the entire film volume; the grain size increases to 20–50 nm.

Figure 2b shows an electron diffraction pattern obtained on a lamella using a TEM. One can see a central white disk and diffraction maxima, located on concentric circumferences. Such a pattern is generally observed when the volume studied contains both amorphous and crystalline regions, with grains misoriented relative to each other.

The measured diffraction ring diameters, distances from the sample to the detecting chamber, and specified electron wavelength λ make it possible to estimate the interplanar spacing in nanocrystals using the Wulff–Bragg's law: $2d\sin\theta = \lambda n$, where d is the interplanar spacing, θ is the diffraction angle, and n is the

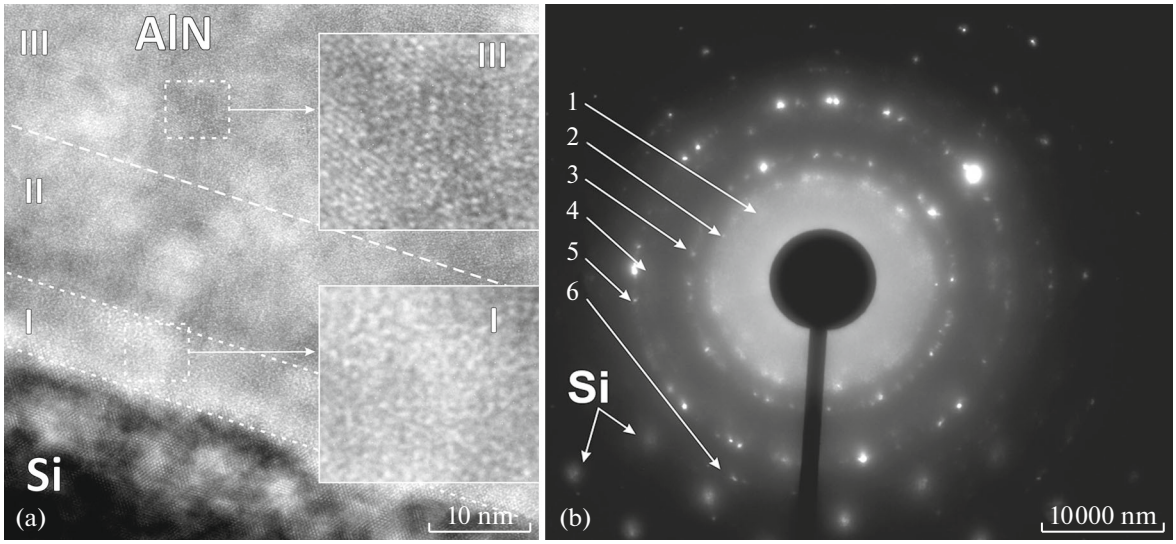

Fig. 2. (a) Cross-sectional TEM image of the sample with a 120-nm-thick AlN film, obtained on a 50-nm-thick lamella. The accelerating voltage is 200 kV. Dashed lines separate amorphous layer I, located on the substrate surface; transition layer II with amorphous and nanocrystalline phases; and nanocrystalline layer III. (b) Electron diffraction pattern obtained on the lamella. The bright disk in the central part is due to the presence of amorphous phase in the film. Numbers 1–6 denote concentric circumferences with diffraction maxima, caused by reflection from families of crystallographic planes. The diffraction maxima due to the silicon substrate are observed in the left bottom corner.

diffraction order. The results of these estimates are presented in Table 1, according to which, rings with numbers 2 and 5 correspond with high accuracy to the second diffraction order from the (0001) and $(10\bar{1}0)$ planes of AlN single crystals with a wurtzite structure [25]. Rings 1 and 6 may be due to the diffraction from the family of $(1\bar{2}10)$ planes of crystalline AlN. However, it is unlikely that rings 3 and 4 are due to the diffraction from an AlN crystal. In accordance with [26], the obtained values of d/n ratios may correspond to the diffraction from the (001), (110), and (120) planes of cubic aluminum oxynitride AlON. High oxygen content in the deposited films was detected by X-ray microanalysis (SEM-EDS). It was found that the oxygen concentration is highest in amorphous layer I (Fig. 2), whose composition is close to alumina Al_2O_3.

Table 1. Calculated d/n ratios for the diffraction rings in Fig. 2b

Ring	d/n, Å	n	Lattice parameters, Å	Material	Plane	D, %
1	2.91	1	$a = 3.11$	AlN	$(1\bar{2}10)$	7
2	2.49	2	$c = 4.98$	AlN	(0001)	1
3	1.93	4	$a = 7.94$	AlON	(001)	3
		3	$\frac{a\sqrt{2}}{2} = 5.61$	AlON	(110)	4
4	1.76	2	$\frac{a\sqrt{2}}{3} = 3.73$	AlON	$(\bar{1}20)$	6
5	1.75	2	$\frac{a\sqrt{5}}{2} = 3.48$	AlN	$(10\bar{1}0)$	1
6	1.48	2	$a = 3.11$	AlN	$(1\bar{2}10)$	5

Relative deviations D of the obtained values of interplanar spacings from the lattice parameters of AlN (wurtzite lattice) [25] and AlON (cubic lattice) [26] single crystals are given (clarification in text).

Results of Electrical Measurements

To estimate the electrical conductivity of deposited AlN films, we measured the I–U characteristics of Au–AlN–(n-Si) structures. At high forward voltages, the space charge region is absent in a semiconductor, and the current is determined by the series resistance of the structure, consisting of the semiconductor substrate and film resistances. The series resistance can be found from the slope of this part of the I–U characteristic. As follows from the data obtained, the resistance of even the thinnest films was several ten times higher than the silicon substrate resistance. Thus, the form of the forward I–U characteristic of the samples studied in the range of high forward voltages was determined by the resistance of the AlN films.

Figure 3 shows the forward I–U characteristic of some investigated samples with AlN films having thicknesses from 2 to 110 nm. As follows from the plots, an increase in the film thickness above 10 nm sharply weakens the forward currents through the structure. Three groups of curves can be selected, which approximately correspond to ranges of thicknesses I (2–10 nm), II (25–35 nm), and III (55–110 nm) (Fig. 2a).

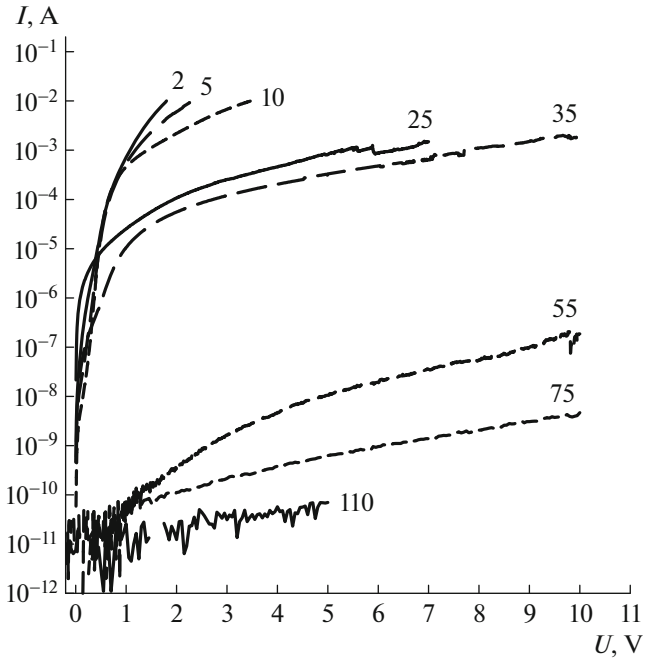

Fig. 3. Forward I–U characteristics of Au–AlN–(n-Si) structures. The AlN film thicknesses (in nm) are indicated near the corresponding curves. The temperature is 294 K.

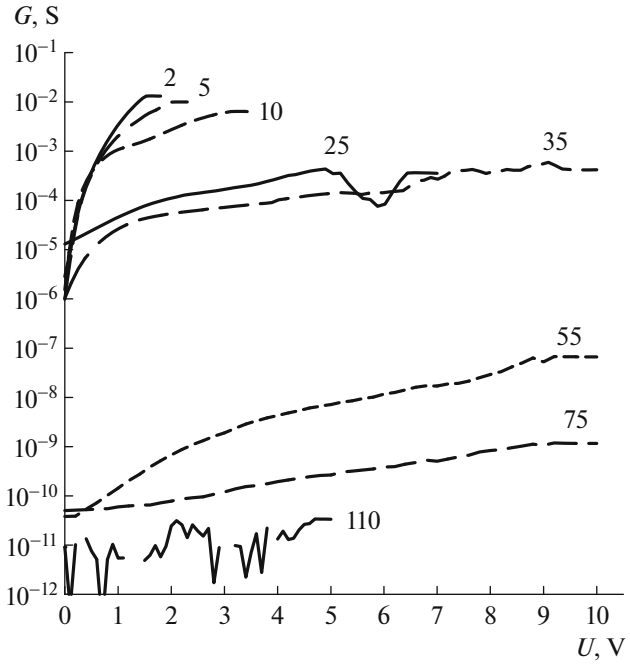

Fig. 4. Dependences of the conductivity on voltage for Au–AlN–(n-Si) structures with different thicknesses of AlN films, calculated from the forward I–U characteristics.

Figure 4 shows the dependences of the structure conductivity G on voltage U, calculated from the I–U characteristics: $G(U) = dI/dU$. One can see that the conductivity of each sample increases with an increase in voltage and reaches a value that barely changes with a further increase in voltage. In correspondence with the above considerations, these values of the sample conductivity were used to calculate the specific conductivity of deposited AlN films.

Figure 5 shows the dependence of the calculated conductivity σ of deposited AlN films on their thickness h: $\sigma = Gh/S$, where S is the contact area. As can be seen in the figure, films with thicknesses of several nanometers had a fairly high conductivity at room temperature. The conductivity rose almost linearly with an increase in film thickness: from 1.5 $(\Omega\ \text{cm})^{-1}$ for $h = 2$ nm to 10 $(\Omega\ \text{cm})^{-1}$ for $h = 15$ nm. However, with a further increase in thickness the film conductivity dropped and amounted to ~3×10^{-7} $(\Omega\ \text{cm})^{-1}$ at $h = 110$ nm. The kink in the characteristic was located in region II at thicknesses ~20 nm.

DISCUSSION

The electron microscopy data demonstrated that the deposited AlN films contained both crystalline and amorphous phases. The amorphous phase was mainly concentrated in thin layer I, adjacent to the substrate surface. As was noted above, the amorphous layer is apparently due to the presence of residual oxygen in the vacuum chamber [9, 16]. The high oxygen concentration in the initial layers of deposited films could cause their amorphization [27, 28]. While the residual oxygen was consumed during gettering by sputtered aluminum, AlN grains have been arising increasingly in the film. In the beginning, rarely located and randomly oriented grains were formed in amorphous layer I. Gradually their location density in the amorphous matrix and their size increased (layer II). With a further decrease in the oxygen concentration the amorphous phase disappeared, and growth of an oriented nanocrystalline AlN film (layer III) began. The observed sequence of layers in the film cross section in Fig. 2a corresponds to the data of [9, 20], where similar images were reported and schematic models of AlN film growth during magnetron sputtering were presented. The estimated oxygen concentrations in an AlN film, where the above-described changes in the film morphology and structure were observed, can be found in [27]. At an oxygen content more than 50%, the film material becomes amorphous; short 5-nm-thick rods arise at 30% oxygen; a columnar texture with many defects and grain thickness of ~10 nm begins be formed at 15% oxygen; and the grains are straightened and their thickness increases to 30 nm at an oxygen content less than 5%. This pattern is also consistent with the results of [29], where it was shown that the AlN grain size increases with a decrease in the oxygen content in the film.

Note that the desorption from chamber walls partially compensates for the oxygen loss caused by gettering. The significant oxygen content in all film layers

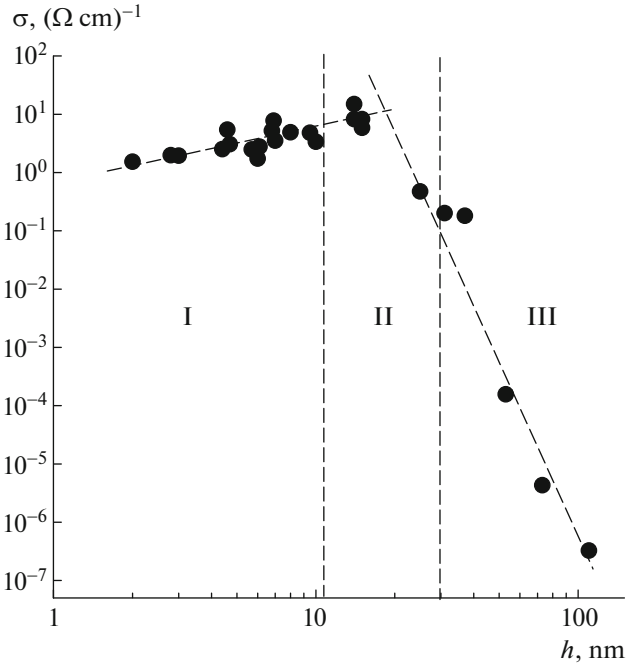

Fig. 5. Dependence of the conductivity on the thickness of deposited AlN films. The temperature is 294 K. Regions I, II, and III, corresponding to the layers in Fig. 2a, are indicated. Dotted lines are the dependences $\sigma(h)$ at thicknesses smaller or larger than 20 nm.

can be explained by this effect. The diffraction pattern in Fig. 2b contains a ring, corresponding to the cubic phase AlON. However, it was shown in [27] that the presence of oxygen in an AlN film (up to 30% concentration) does not lead to the formation of crystalline or amorphous AlON phase. Only the crystalline AlN phase with a wurtzite structure is recorded. This contradiction requires additional structural studies of AlN films obtained by RMS.

The influence of oxygen on the crystal structure of AlN single crystals was investigated in [30–36], where it was found that oxygen is a substitutional impurity at concentrations below 1%. When nitrogen is replaced with oxygen, aluminum vacancies are formed to preserve the charge balance in the lattice; along with oxygen atoms, these vacancies become correlated point defects [30–32]. When the oxygen concentration increases to 6%, aluminum, oxygen, and nitrogen form octahedral inclusions, which are structural units of planar defects: inversion domain boundaries (IDBs), dividing domains with a specularly symmetric structure [33–36]. Generally, IDBs lie in the basal plane, but they may bend and pass into the prismatic plane of wurtzite lattice. IDBs are extended lattice defects [34–36]. Specifically defects of this type (IDBs, jointly with grain boundaries) can be responsible for the higher electrical conductivity of polycrystalline samples in comparison with single crystals [37, 38].

The AlN films investigated in this study, whose thicknesses are below 20 nm, are characterized by a high oxygen content and, as a consequence, a small size of crystallites and a high density of their boundaries. This circumstance may explain their high conductivity (see Fig. 5). An increased conductivity along grain boundaries was found in undoped polycrystalline diamond films [39]. An analysis of the temperature and frequency dependences of the conductivity suggested that the carrier transport occurs according to the hopping mechanism, which is implemented at high density of electronic states at boundaries. Yanev et al. [40] observed a high current density at grain boundaries in nanocrystalline $HfSi_xO_y$ and ZrO_2 films using scanning tunnel microscopy; its value significantly exceeded the bulk current density.

According to the aforesaid, one can suggest that the rise in the conductivity in the initial portion of the curve (Fig. 5), at thicknesses from 2 to 20 nm, may be due to the increase in the density of grain boundaries because of the increase in the number of grains and their increasing proximity in the amorphous matrix with increasing oxygen consumption in the chamber. At small film thicknesses many grains grow from the substrate to the film surface, and the current transport can freely be performed along their boundaries. With a further decrease in the oxygen concentration, crystallites begin to increase in size, they occupy the entire film volume, and the boundary density begins to decrease. Thus, the zone of nanocrystalline film growth is located on the right from the point of maximum in the dependence of conductivity on thickness (Fig. 5), and the zone of mixed (amorphous and nanocrystalline) growth is located on the left.

Note that many grains in the 150-nm AlN film (Fig. 1d) do not penetrate through it, resting against the boundaries of subsequent grains. In the case of current flow through such a medium, carriers must overcome the barriers existing at grain boundaries, as a result of which the film resistance significantly increases [37]. A high density of electronic states at grain boundaries [37, 38] may lead to capture of free carriers and manifest itself in the form of enhanced level of charge loss and noise in an MIS structure containing a nanocrystalline film.

CONCLUSIONS

The AlN films deposited by RMS on silicon substrates contained both crystalline and amorphous phases. Most of the amorphous phase was concentrated in a thin layer up to 10 nm thick, adjacent to the substrate surface. The occurrence of an amorphous layer is believed to be due to the presence of residual oxygen in the vacuum chamber. While oxygen was consumed because of the sputtered aluminum gettering, the film structure changed from amorphous to nanocrystalline. AlN films with thicknesses up to

20 nm had a high conductivity: up to 10 $(\Omega\ \text{cm})^{-1}$, which was apparently due to the high density of grain boundaries in the amorphous matrix. With an increase in thickness above 20 nm the film conductivity dropped to values of $\sim 10^{-7}$ $(\Omega\ \text{cm})^{-1}$, following the decrease in the grain boundary density. To understand the mechanism of current transport in the obtained AlN films, additional measurements of the dependences of their electrical conductivity on temperature and electric field should be performed. Separate studies are needed to establish the influence of the substrate conductivity type on the conductivity of AlN films several nanometers thick, when the substrate effect may be most pronounced.

ACKNOWLEDGMENTS

We are grateful to the colleagues of the Interdisciplinary Resource Center for Nanotechnology of St. Petersburg State University for the help in studying the morphology and structure of the samples using SEM and TEM.

FUNDING

This work was supported by ongoing institutional funding. No additional grants to carry out or direct this particular research were obtained.

CONFLICT OF INTEREST

The authors of this work declare that they have no conflicts of interest.

REFERENCES

1. A. M. Ivanov, N. B. Strokan, I. M. Kotina, et al., Tech. Phys. Lett. **35** (5), 459 (2009). https://doi.org/10.1134/S1063785009050228
2. A. M. Ivanov, I. M. Kotina, M. S. Lasakov, et al., Semiconductors **44** (8), 1030 (2010). https://doi.org/10.1134/S1063782610080130
3. H.-Ch. Lee, G.-H. Kimb, S.-K. Hong, et al., Thin Solid Films **261**, 148 (1995).
4. I. C. Oliveira, K. G. Grigorov, H. S. Maciel, et al., Vacuum **75**, 331 (2004). https://doi.org/10.1016/j.vacuum.2004.04.001
5. T. P. Drusedau and J. Blasing, Thin Solid Films **377–378**, 27 (2000).
6. M. Clement, E. Iborra, J. Sangrador, et al., J. Appl. Phys. **94**, 1495 (2003). https://doi.org/10.1063/1.1587267
7. M. A. Signore, E. Bellini, A. Taurino, et al., J. Phys. Chem. Solids **74**, 1444 (2013). https://doi.org/10.1016/j.jpcs.2013.05.003
8. J. H. Choi, J. Y. Lee, and J. H. Kim, Thin Solid Films **384**, 166 (2001).
9. B.-H. Hwang, Ch.-Sh. Chen, H.-Y. Lu, and T.-Ch. Hsu, Mater. Sci. Eng. **325**, 380 (2002).
10. W.-J. Liu, Sh.-J. Wu, Ch.-M. Chen, et al., J. Cryst. Growth **276**, 525 (2005). https://doi.org/10.1016/j.jcrysgro.2004.11.421
11. J. X. Zhang, Y. Z. Chen, H. Cheng, et al., Thin Solid Films **471**, 336 (2005). https://doi.org/10.1016/j.tsf.2004.06.161
12. G. W. Auner, F. Jin, V. M. Naik, and R. Naik, J. Appl. Phys. **85**, 7879 (1999). https://doi.org/10.1063/1.370600
13. M. Ishihara, S. J. Li, H. Yumoto, et al., Thin Solid Films **316**, 152 (1998).
14. T. Adam, J. Kolodzey, C. P. Swann, et al., Appl. Surf. Sci. **175–176**, 428 (2001).
15. G. F. Iriarte, F. Engelmark, and I. V. Katardjiev, J. Mater. Res. **17** (6), 1469 (2002).
16. V. Brien and P. Pigeat, J. Cryst. Growth **299**, 189 (2007). https://doi.org/10.1016/j.jcrysgro.2006.10.238
17. E. Yarar, V. Hrkac, C. Zamponi, et al., AIP Adv. **6**, 075115 (2016). https://doi.org/10.1063/1.4959895
18. X.-H. Xu, H.-Sh. Wu, C.-J. Zhang, and Zh.-H. Jin, Thin Solid Films **388**, 62 (2001).
19. H. Y. Liu, G. S. Tang, F. Zeng, and F. Pan, J. Cryst. Growth **363**, 80 (2013). https://doi.org/10.1016/j.jcrysgro.2012.10.008
20. W.-J. Liu, Sh.-J. Wu, Ch.-M. Chen, et al., J. Cryst. Growth **276**, 525 (2005). https://doi.org/10.1016/j.jcrysgro.2004.11.421
21. M. A. Signore, A. Taurino, D. Valerini, et al., J. Alloys Compd. **649**, 1267 (2015). https://doi.org/10.1016/j.jallcom.2015.05.289
22. A. Fathimulla and A. A. Lakhani, J. Appl. Phys. **54**, 4586 (1983). https://doi.org/10.1063/1.332661
23. O. Elmazria, M. B. Assouar, P. Renard, and P. Alnot, Phys. Status Solidi A **196** (2), 416 (2003). https://doi.org/10.1002/pssa.200306446
24. R. Schmidt, P. Mayrhofer, U. Schmid, and A. Bittner, J. Appl. Phys. **125**, 084501 (2019). https://doi.org/10.1063/1.5050181
25. *Powder Diffraction File* (JCPDS International Centre for Diffraction Data, PA, 1998). https://www.icdd.com/pdfsearch/.
26. N. D. Corbin, J. Eur. Cer. Soc. **5**, 143 (1989).
27. V. Brien and P. Pigeat, J. Cryst. Growth **310**, 3890 (2008). https://doi.org/10.1016/j.jcrysgro.2008.06.021
28. A. Von Richthofen and R. Domnick, Thin Solid Films **283**, 37 (1996).
29. L. Vergara, M. Clement, E. Iborra, et al., Diam. Relat. Mater. **13**, 839 (2004). https://doi.org/10.1016/j.diamond.2003.10.063
30. G. A. Slack, J. Phys. Chem. Solids **34**, 321 (1973).
31. G. A. Slack, R. A. Tanzilli, R. O. Pohl, and J. W. Vandersande, J. Phys. Chem. Solids **48** (7), 641 (1987).
32. G. A. Slack, L. J. Schowalter, D. Morelli, and J. A. Freitas, Jr., J. Cryst. Growth **246**, 287 (2002).

33. J. H. Harris, R. A. Youngman, and R. G. Teller, J. Mater. Res. **5** (8), 1763 (1990). https://doi.org/10.1557/JMR.1990.1763

34. A. D. Westwood, R. A. Youngman, M. R. McCartney, et al., J. Mater. Res. **10** (5), 1270 (1995). https://doi.org/10.1557/JMR.1995.1270

35. A. D. Westwood, R. A. Youngman, M. R. McCartney, et al., J. Mater. Res. **10** (5), 1287 (1995). https://doi.org/10.1557/JMR.1995.1287

36. A. D. Westwood, R. A. Youngman, M. R. McCartney, et al., J. Mater. Res. **10** (10), 2573 (1995). https://doi.org/10.1557/JMR.1995.2573

37. H. F. Matare, J. Appl. Phys. **56**, 2605 (1984). https://doi.org/10.1063/1.333793

38. H. F. Matare, J. Appl. Phys. **59**, 97 (1986). https://doi.org/10.1063/1.336846

39. B. Fiegl, R. Kuhnett, M. Ben-Chorin, and F. Koch, Appl. Phys. Lett. **65**, 371 (1994). https://doi.org/10.1063/1.112379

40. V. Yanev, M. Rommel, M. Lemberger, et al., Appl. Phys. Lett. **92**, 252910 (2008). https://doi.org/10.1063/1.2953068

Translated by Yu. Sin'kov

Publisher's Note. Pleiades Publishing remains neutral with regard to jurisdictional claims in published maps and institutional affiliations.